Analyst

Accepted Manuscript

ROYAL SOCIETY OF CHEMISTRY

www.rsc.org/analyst

Spatial Organization of *Pseudomonas aeruginosa* Biofilms Probed by Combined Matrix-Assisted Laser Desorption Ionization Mass Spectrometry and Confocal Raman Microscopy

Rachel N. Masyuko[a], Eric J. Lanni[b], Callan M. Driscoll[c], Joshua D. Shrout[c], Jonathan V. Sweedler[b*] and Paul W. Bohn[a,d*]

[a]Department of Chemistry and Biochemistry, University of Notre Dame, Notre Dame, IN 46556

[b]Department of Chemistry, University of Illinois at Urbana-Champaign, 600 S. Mathews Ave., Urbana, IL 61801

[c]Department of Civil and Environmental Engineering and Earth Sciences, University of Notre Dame, Notre Dame, IN 46556

[d]Department of Chemical and Biomolecular Engineering, University of Notre Dame, Notre Dame, IN 46556

[*]Authors to whom correspondence should be addressed, *pbohn@nd.edu*, *jsweedle@illinois.edu*

Abstract

Bacteria growing as surface attached biofilms differ significantly from planktonic cells in several important traits that are reflected in the spatiotemporal organization of the cells and the extracellular polymeric substances they secrete. The structural and chemical features that define these biofilms are explored here using a combination of matrix-assisted laser desorption ionization mass spectrometry (MALDI MS) and confocal Raman microspectroscopies (CRM) to characterize and compare the composition and distribution of biomolecules found in biofilms and planktonic cells of the bacterium *Pseudomonas aeruginosa*. Three-day old *P. aeruginosa* biofilms show dramatic differences in molecular composition compared to planktonic cultures. CRM reveals that wild-type planktonic cell Raman spectra are characterized by bands linked to cellular constituents and are dominated by contributions from DNA- and RNA-related bands. In contrast, biofilm spectra are dominated by bands characteristic of glycolipids – rhamnolipids – polysaccharides and by secreted proteins. LDI MS was applied in turn to identify the rhamnolipids present in the biofilm. Experiments were also conducted using an acyl homoserine lactone quorum sensing-deficient mutant (Δ*las*Δ*rhlI*), which is incapable of producing rhamnolipids. CRM and LDI MS analyses revealed that while molecular composition of the planktonic quorum sensing-deficient cells is similar to that of the wild-type planktonic cells, several compositional differences are observed in the mutant after biofilm growth, including complete absence of detectable rhamnolipids. CRM vibrational spectra of the mutant cells are very similar for planktonic and biofilm growth conditions, indicating that biofilm formation is greatly hindered in the absence of functioning quorum sensing machinery.

Introduction

Biofilm bacteria are encased in a self-produced matrix formed by extracellular polymeric substances (EPS), which make up most of the biofilm organic matter by mass.[1] EPS are comprised of complex mixtures of macromolecules, such as proteins, polysaccharides, nucleic acids, lipids and amphiphilic polymers.[2, 3] The nature of the EPS is not only complex, but dynamic; the molecules within the EPS are known to interact with each other and promote various functions such as biofilm formation, structural stabilization, sequestration of nutrients and water, and protection of the embedded microbes from environmental perturbations.[3] Acting in concert with the functions of the EPS, bacteria within biofilms form a complex microbial community that can exhibit primitive homeostasis, a circulatory system, and metabolic cooperativity,[4] often conveying beneficial effects for the population.

Biofilms themselves can be either beneficial or harmful to humans; they are beneficial in biotechnology applications, such as wastewater treatment[5] and chemical production, *e.g.* through fermentation in biofilm-based bioreactors.[6] On the other hand, bacteria within biofilms can be up to 1000 times more resistant to antibacterial treatments than planktonic cells.[7] Recent studies have inferred that antimicrobial resistance in biofilms is multifactorial, being ascribed to a combination of mechanisms.[8] In addition, consistent with the obvious phenotypic differences, biofilm bacteria show different gene expression profiles than planktonic bacteria[9, 10] and respond differently to environmental perturbations than their planktonic counterparts.[11]

Pseudomonas aeruginosa is a Gram-negative bacterium that is ubiquitous in the natural environment and is present in many engineered systems.[12-14] A factor linked to *P. aeruginosa* biofilm formation is the inter-cellular signaling cascade known as quorum sensing (QS),[15, 16]

which is mediated by two acyl homoserine lactone (AHL) QS systems, *las* and *rhl*, each system having its own signal synthase, signal receptor and AHL signal transmission system. The signals for the *las* and *rhl* systems are 3-(oxo-dodecanoyl)-homoserine lactone and the N-butaryl-homoserine lactone.[16, 17] *P. aeruginosa* is known to cause infections in burn wound patients,[18] patients with cancer,[19] HIV,[20] and cystic fibrosis,[21] with AHL quorum sensing linked with several pathogenic traits.[22] In most cases, biofilm-related behavior of *P. aeruginosa* is strongly associated with its pathogenic effects.[23] Yet questions remain concerning the spatial and dynamic expression of AHL quorum sensing *in vivo*—the uniform quorum sensing response(s) observed in studies of planktonic cultures can be markedly less uniform when considering *P. aeruginosa* strain or surface growth differences.[24-27]

Clearly, the ability to distinguish bacterial cells along a path - from initially surface-adhered planktonic cells, through the formation of microcolonies to encasement in an extracellular polymeric matrix that signals a fully developed biofilm - is of utmost importance, and methods based on molecular composition exhibit great promise in the management of biofilms, whether in the environment or in a health care context. While pathogenic microorganisms are typically identified using biochemical tests, these can take days to complete, [28] and it is essential to characterize not only the bacteria but the deleterious biofilms. Biofilm formation in *P. aeruginosa* can be analyzed through a combination of molecular genetics, phenotype characterization and signaling pathway analysis.[29-31] However, given the complex nature of biofilms, techniques with multiplex analysis capabilities, such as mass spectrometry and vibrational spectroscopy, are alternatives with great potential. Microspectroscopies can be used for rapid identification and characterization of complex microbial systems, while mass

spectrometric and vibrational imaging modalities can provide additional information on the spatial distribution of characteristic molecular constituents that define a biofilm and its behavior. Furthermore, these two approaches are well-matched; vibrational spectroscopy provides a global analysis of the sample at the level of chemical functional groups, while mass spectroscopy identifies the biofilm constituents.

Vibrational Raman and infrared spectroscopies are non-destructive, label-free techniques that provide functional group information on a large number of cellular components. While the strong absorption of water in the mid-IR limits its usage to specialized applications such attenuated total reflectance IR microscopy in this spectral region, Raman spectroscopy is not affected by water, because it scatters weakly. With these natural advantages, Raman spectroscopy has been used to probe a wide range of both prokaryotic and eukaryotic cells,[32-34] to characterize bacteria and biofilms,[35-39] including medically relevant bacteria,[40] and for structural analysis of cellular components.[41] Raman scattering coupled with confocal microscopy affords three dimensional imaging at high spatial resolution and has been utilized for single cell mapping and analysis.[37, 42]

Mass spectrometry (MS) is a nearly ideal complement to Raman imaging, because it yields highly specific chemical information – molecular weight – of sample components which can be ionized. Ions can be further characterized by structural analysis through tandem MS experiments, which is especially useful for identifying unknown species and confirming mass assignments. The selection of ion source significantly affects the molecular classes that can be ionized and defines the physical process of ion generation; direct ionization from solid surfaces is possible with microprobe ion sources such as focused lasers, *e.g*. matrix-assisted laser desorption/ionization, MALDI, and ion beams, *e.g*. secondary ion mass spectrometry, SIMS,[43]

which enables *MS profiling* – sampling of micro-scale regions on a large sample surface to obtain spatially specific chemical information. Taken a step further, multiple MS profiles can be acquired in a rectangular array of points over an extended area. This technique, known as *MS imaging* (MSI), maps the distribution of all detected ions within a specified area. Each MS profile is treated as a single pixel in the MSI experiment, and ion images are generated by defining pixel brightness to indicate the relative intensity of a selected ion at that position in the sample. MSI is a powerful, multiplex, and label-free imaging technique which can visualize many molecules which are not easily labeled, notably lipids and other small metabolites. Thanks to these characteristics, MSI is now employed routinely in biological and clinical research fields at macroscopic (tissue-level) [44] and microscopic (cell/subcell) size scales,[45] including in microbiology where it has been used to study interspecies metabolic interactions,[46] biofilm secretion,[47] and subcellular molecular distributions [48] among other applications.[49]

In the present study, static biofilms prepared from both wild-type *P. aeruginosa* and an isogenic QS mutant deficient for both AHL signal production and rhamnolipid secretion are spatially analyzed using both confocal Raman microscopy (CRM) and MALDI MSI. Raman and MS spectral profiles and images acquired from the biofilm are compared to those of the corresponding planktonic cells in order to examine the changes in composition associated with biofilm formation. While the wild-type *P. aeruginosa* biofilms show the presence of glycolipids and increased protein excretion, analysis of the QS deficient cells do not show any of these changes. In fact, the molecular composition is similar for both planktonic and biofilm growth conditions. Combining CRM and MSI allows data to be cross validated, as well as providing complementary chemical information.[50, 51] CRM detects molecular classes that are not efficiently

ionized by MS, while MSI can resolve multiple rhamnolipid species[52, 53] in the wild-type biofilm which give rise to a single peak in the Raman spectrum. Confirmation of their identities by *in situ* tandem MS shows that rhamnolipid congeners exhibit different distributions across the biofilm surface, a feature which may relate to their functions and/or expression within the biofilm.

Experimental

Biofilm preparation. *Pseudomonas aeruginosa* ATCC strain 15692 and an isogenic QS mutant deficient for AHL production and for rhamnolipid excretion (Δ*las*Δ*rhlI*) [54] were used in all experiments. Cells were grown overnight at 30°C using sterilized FAB medium[55] with 150 µL of 1.2 M filter-sterilized glucose as a carbon source to an optical density (OD) of 1.0 at 600 nm. The FAB medium contained the following components: $(NH_4)_2SO_4$ (2 g L^{-1}), Na_2HPO_4. $2H_2O$ (6 g L^{-1}), KH_2PO_4 (3 g L^{-1}), NaCl (3 g L-1), $MgCl_2$(93 mg L^{-1}), $CaCl_2$(11 mg L^{-1}) and trace metals solution (1 ml L^{-1}). The trace metals solution contained $CaSO_4$. $2H_2O$ (200 mg L^{-1}), $FeSO_4$.7H2O (200 mg L^{-1}), $MnSO_4.H_2O$ (20 mg L^{-1}), $CuSO_4$. $5H_2O$ (20 mg L^{-1}), $ZnSO_4$. $7H_2O$ (20 mg L^{-1}), $CoSO_4.7H_2O$ (10 mg L^{-1}), $NaMoO_4$. H_2O (10 mg L^{-1}), H_3BO_3 (5 mg L^{-1}). Planktonic cells were centrifuged and washed three times in phosphate buffered saline (PBS) then placed on (100) silicon for both Raman and MS analysis. Biofilms were grown on 2 cm x 2 cm pieces of (100) Si placed at the bottom of Petri dishes. For biofilm growth, the cell culture solution was deposited onto the Si wafers at the bottom of the Petri dish, and additional growth medium with 450 µL of 1.2 M glucose was added at a volume ratio of 1:49 (cell culture: growth medium). Biofilms were

allowed to develop at 30°C for 72 h. Extra growth medium was pipetted from the Petri dish and the silicon-supported biofilms were dried at 25°C for 12 h in a sterile environment prior to analysis. Additional samples were prepared on Au-coated (100) Si for Raman analysis in order to expose any peaks that might overlap and be obscured by the strong ν(Si-O) band from SiO_2. Gold-coated substrates were prepared by thermally evaporating a 3 nm Cr adhesion layer followed by 100 nm of Au onto a clean (100) Si wafer.

Confocal Raman Measurements. Raman spectra were acquired at 300 K using a confocal Raman microscope (Alpha 300R, WITec GmbH, Germany) equipped with a focused Nd:YAG laser operating at the second harmonic frequency (λ = 532 nm) and a 60x, coverslip-corrected Nikon water-immersion objective (NA=1.0). Laser radiation was delivered via a single mode optical fiber through a dichroic beam splitter into the microscope objective and focused onto the sample. The scattered Raman radiation was collected by the same objective and focused into a 50 μm diameter multi-mode fiber connected to a UHTS 300 spectrometer equipped with a 600 groove mm^{-1} grating and a back-illuminated CCD camera (Newton DU970 N-BV, Andor Inc., cooled to -65°C). Each Raman spectrum was recorded by accumulating 100 spectra at an integration time of 0.5 s each at 15 mW incident laser power. On each sample, individual Raman spectra were collected at 25 spatial locations and averaged to produce representative spectra for that sample. Raman images were acquired by recording a full Raman spectrum at every pixel (150 x 150 array for a total of 22,500 spectra per image) over the desired surface area at an integration time of 100 ms. The step sizes (not spatial resolution) for the images reported in this work are 33 nm, 170 nm and 210 nm for Figs. 3(a), 3(b), and 3(c) respectively. Raman images showing the distribution of various constituents were calculated by integrating the area under the

corresponding Raman band. WITec software was used for Raman data analysis. Raman spectra were baseline corrected using a fourth order polynomial function.

Mass Spectrometry Measurements. For all MALDI MS experiments, biofilms and planktonic cell samples were grown or deposited on uncoated silicon wafers and dried as described in the Biofilm Preparation section, then processed by applying a 1-2 nm thick Au layer to the surface with a Desk II TSC sputter coater (Denton Vacuum, Moorestown, NJ, USA) run for 6 s at 40% power and 65 mTorr of Ar. The biofilm-coated silicon wafers were then affixed with double-sided conductive tape (Electrical Tape, 3M, St. Paul, MN, USA) to a custom stainless steel MALDI target modified with a shallow cutout to precisely level the silicon wafer surface with the plate face, a step which was critical to obtaining high quality mass spectra from the biofilms. All MS experiments were performed on an Ultraflextreme MALDI-TOF/TOF MS (Bruker Daltonics, Billerica, MA, USA) set to reflectron/positive ion mode with matrix suppression disabled, using a frequency-tripled Nd:YAG Smartbeam II laser. Imaging experiments were performed with *m/z* range 20-1000, "medium" laser size (~100 μm probe diam. estimated by matrix ablation), 1000 Hz frequency, 200 shots/position, and 500 μm step/pixel size. Quadratic calibration was performed using K^+ and Au_n^+ cluster ions. Tandem MS (TOF/TOF) experiments were performed in post-source decay mode (without CID), and laser power was adjusted for each parent ion to maximize fragmentation. Data was processed using flexAnalysis v3.4 and flexImaging v3.0; ion filters were ±0.25 Da and images were RMS-normalized. Mixed rhamnolipid standard (95%, Aldrich) was purchased from Sigma Aldrich (St. Louis, MO, USA).

Results and Discussion

Confocal Raman Analysis. *P. aeruginosa* biofilms grown under static conditions on Si and Au-coated Si wafers were initially analyzed using Raman microspectroscopy. Fluorescence imaging experiments, Figs. S1(a) and (b), confirmed that biofilms grown on both Au and Si were similar. The specific Raman spectra observed here represent an ensemble of signals that arise from the molecular vibrations of individual cell components, integrating over lipids, proteins, nucleic acids and carbohydrates. Raman measurements for both wild type and mutant strains were performed in water. Autofluorescence, which is ubiquitous in biological materials, is significantly reduced in water, thus substantially reducing the background. Also the refractive index of water, $n = 1.33$, is close to that of bacterial cells and media, thereby minimizing refraction-induced image distortion effects. Finally, water efficiently dissipates the heat generated from laser irradiation, thus limiting potential thermal damage to the samples. Thus, the ability to perform confocal Raman imaging in water yields substantial experimental advantages in comparison to infrared vibrational imaging. Raman spectra of *P. aeruginosa* wild type and QS-mutant planktonic cells and biofilms were acquired between 100 cm^{-1} and 3600 cm^{-1}, however, the studies reported here concentrate on vibrational bands found in the fingerprint region 600 – 1800 cm^{-1}. Outside this range, C-H stretching vibrations in the range 2750 - 3050 cm^{-1} dominate spectra. Although these bands carry important information about cell membrane fluidity,[56, 57] this information is of less interest here.

Figure 1 compares the Raman spectrum in the vibrational fingerprint region from planktonic cells, Fig. 1(a), to that of a biofilm grown from the same planktonic cells, Fig. 1(b). The Raman spectrum of wild type *P. aeruginosa* in the planktonic state, Fig. 1(a), exposes vibrational bands that belong to the basic biological building blocks of the cell, with the nucleotide bases

dominating under the conditions used here. The Raman spectrum reveals a series of DNA/RNA base vibrations that are well defined, the strongest of these being the characteristic thymine out-of-plane C-O bending vibration at ~747 cm^{-1}, along with the guanine and adenine ring breathing vibrations observed in a well-defined high intensity band at 1585 cm^{-1}.[58] Strong bands at 1126 cm^{-1} and 1310 cm^{-1} along with the medium intensity band at 1336 cm^{-1} are assigned to cytosine and the adenine ring breathing vibration,[59] and a weaker band at 783 cm^{-1} represents the ring distortions from both cytosine and uracil with a contribution from the O-P-O symmetric vibrational stretch.[41, 60] The spectrum also shows bands that belong to proteins, carbohydrates and lipids that are significantly weaker than the DNA/ RNA bands. Protein bands at 1170 cm^{-1} and 1223 cm^{-1} are assigned to tyrosine C-H in plane bending vibrations and amide III vibrations,[61] and the band at 1358 cm^{-1} arises from the indole ring stretch of tryptophan. The band at 1448 cm^{-1} is representative of CH_2 scissoring deformation vibrations that arise from proteins, carbohydrates and lipids.[59]

Upon biofilm formation, dramatic changes occur in the spectrum, Fig. 1(b). Biofilms cultivated on bare Si exhibit a greatly reduced SiO_2 background (915-1015 cm^{-1}), presumably because biofilms at 72 h are much thicker than the < 1 μm confocal depth of the CRM. In addition, the strong DNA/RNA-related bands at 747 (thymine), 1126 (cytosine), and 1310 cm^{-1} (adenine) are all greatly diminished or disappear altogether. The only DNA/ RNA contributions remaining in the biofilm spectrum are very weak bands at 792 cm^{-1} attributed to cytosine and uracil ring stretching vibrations and a 1507 cm^{-1} band assigned to adenine. The strong band at 1585 cm^{-1} is reduced in strength and a new band at 1601 cm^{-1} grows in. In addition, narrow bands with peaks centered at 999 cm^{-1} and 1030 cm^{-1} appear as well as smaller bands centered at 1068 cm^{-1}, 1097

cm^{-1}, 1155 cm^{-1} and 1197 cm^{-1}. Most striking is the intense peak at 999 cm^{-1} attributed to symmetric ring breathing vibrations in phenylalanine and tryptophan, indicative of proteins.[62] Other bands characteristic of proteins are the broad band at 1175-1235 cm^{-1} that can be attributed to C-H in plane bending vibrations in tyrosine and phenylalanine, amide III and C-C_6H_5 stretching vibrations[61] and the two bands at 617 cm^{-1} and 1601 cm^{-1} arising from in plane ring breathing deformation and C=C stretching vibrations in phenylalanine.[62] The presence of these bands shows that the composition of the biofilm is different than that of the planktonic cells. More specifically, the contribution from proteins is significantly increased, as indicated by the relative intensities of the protein-characteristic bands compared to those derived from DNA/RNA, unlike planktonic cells where DNA/RNA peaks are dominant. These observations are consistent with the growth of a relatively thick biofilm, which dilutes the contribution of cellular nucleotide-derived peaks. The changes shown in the relative intensities of nucleic acid and protein bands in the planktonic and biofilm spectra in this case are consistent with other studies that have shown that bacteria produce more RNA when entering the logarithmic growth phase. This contrasts with a decrease in RNA levels and increase in protein when bacteria slow their growth and enter the stationary phase, a change that is reflected in the Raman bands characteristic of nucleotide-bases.[63, 64] These observations also reflect the RNA increases associated with the growth cycle of bacteria described previously by Herbert.[65]

The important band at 1030 cm^{-1}, as well as bands at 1068 cm^{-1}, 1095 $cm^{-1}$and 1155 cm^{-1}, lie in the carbohydrate region of the spectrum, and are observed in the wild type biofilm spectrum, Fig. 1(b), but not in the spectrum from the planktonic cells, Fig. 1(a). These are classified as C-O stretching (1030 cm^{-1}), C-C and C-O stretching (1068 cm^{-1}), C-O-C glycosidic link symmetric

ring breathing (1095 cm^{-1}) and C-C and C-O asymmetric ring breathing (1155 cm^{-1}) vibrations.[58-60] In the context of *Pseudomonas*-derived biofilms, these bands suggest the presence of rhamnolipids,[66] a specific class of glycolipids known to be secreted by *Pseudomonas* species concurrently with biofilm formation,[67, 68] an assignment confirmed via MS. Comparison of representative microspectra from a *Pseudomonas* wild-type biofilm, Fig. 1(b) with a mixed rhamnolipid standard shows that the standard has contributions from common Raman bands at 1030 cm^{-1}, 1068 cm^{-1}, and 1155 cm^{-1} characteristic of the sugar moieties, as described above, and consistent with the presence of rhamnolipids in the biofilm matrix. Confirming the assignment of these bands to rhamnolipids, the MS data below not only show the presence of rhamnolipids, but allow their assignment to individual congeners.

Figure 2 shows representative microspectra from the isogenic QS Δ*las*Δ*rhlI* mutant, a strain which is also deficient for rhamnolipid production, since QS is required for rhamnolipid production.[69] Figure 2(a) shows planktonic cell spectra, and Fig. 2(b) shows spectra for the QS (rhamnolipid-deficient) mutant obtained using the conditions used to grow biofilms from the wild-type strain. The first striking feature in comparison to Fig. 1, is that the DNA/RNA bands at 747, 1126, 1310, 1447, and 1585 cm^{-1} present in the planktonic cell spectrum are also observed in the 72 h spectrum, *i.e.* sufficient time for biofilm development in the wild-type, Fig. 1(b). In addition, the rhamnolipid bands clearly observed at ~1030 cm^{-1}, 1068 cm^{-1} and 1155 cm^{-1} in Fig. 1(b) are absent in Fig. 2(b). Both indicate that biofilm development is hindered, or even completely absent, in the QS mutant.

To further elucidate the compositional and structural changes accompanying biofilm formation, Raman images in different scattering windows were acquired and are shown in Fig. 3(a) for

planktonic cells and Fig. 3(b) for the biofilm. The image in Fig. 3(a), assembled from ν(C-H) stretching vibrations in the 2800-3050 cm^{-1} window (representative of all organic matter), was acquired from *P. aerguinosa* wild-type planktonic cells on a surface and shows distinct cell bodies, ostensibly in different orientations. To show the distribution of the different molecular species on the biofilm surface, Raman images were constructed from 2800-3050 cm^{-1} (all organic matter), 1560-1620 (proteins), and 1010-1165 cm^{-1} (carbohydrates and glycolipids), as shown in Fig. S2. A composite image showing the distribution of glycolipid and carbohydrate molecular components 1010-1165 cm^{-1} scattering (blue) and protein 1560-1620 cm^{-1} scattering (red) is shown in Fig. 3(b). This image is clearly dominated by scattering from secreted metabolites on the surface. Figure 3(c) shows a cross-sectional image in the *x-z* orientation of a biofilm assembled from 2800-3050 cm^{-1} (red) showing distribution of all organic components, 1560-1620 cm^{-1} (blue) representing protein species and 725-775 cm^{-1} (green), the latter region capturing the 747 cm^{-1} band assigned to thymine, meaning that this component is representative of DNA components found within the cell. The cross-sectional image clearly shows that the cell-derived nucleotide components are not visible on the surface of the biofilm but rather are found deep within the biofilm, below the protein/carbohydrate-rich EPS matrix. This observation is consistent with bacterial cells constituting a relatively small portion of the biofilm mass.

Mass Spectrometry. MALDI MS is commonly performed by coating the sample surface with a solution of organic acid, but here a thin coating of gold was used as the matrix, *i.e.* metal-enhanced LDI, or "MetA-LDI",[70, 71] which typically limits mass range to < 1 kDa and thus excludes analysis of intact proteins but also yields several advantages for this work, *e.g.* virtually no matrix interference below *m/z* 1000, internal calibration on Au_n^+ cluster ions in the same

range, and a highly uniform, easily-reproducible coating. Au thickness was initially optimized by coating and imaging rhamnolipid standard dried on silicon (Fig. S3) which showed that the thinnest possible uniform coating, *ca*. 2 nm thick, yields the strongest signal. On biofilms prepared here, this preparation routinely allowed detection of over two hundred ions within *m/z* 20-1,000 per microprobe location (image pixel) on the sample. The focus of this work was on profiling rhamnolipids as discussed below, but other known *P. aeruginosa* primary and secondary metabolites are also likely detected within this mass range and can therefore be studied using the same approach in future work.

Typical single pixel spectra of *P. aeruginosa* wild-type biofilm, wild-type planktonic cells, and QS mutant biofilm are shown in Fig. 4. Notably, major spectral features detected exclusively in the wild-type biofilm include several ions in the *m/z* 350-800 range which are identified as rhamnolipid salt adducts based initially on mass match with previous analyses of *P. aeruginosa* bulk extracts by MALDI [72] and LC-ESI MS.[73] To confirm these mass assignments, *in situ* tandem MS was performed, and spectra were matched with expected molecular fragments as well as spectra acquired from rhamnolipid standards (spectra shown in Fig. S4).[74] Nine unique putative rhamnolipid species were detected on the wild-type biofilm and of these, six were detected with sufficient intensity for confirmation by tandem MS; ion identification data are listed in Table 1 using standard rhamnolipid nomenclature.[73]

While this is a small fraction of the many dozens of molecular species reported for *P. aeruginosa* in total,[73] it is in good agreement with the subset previously detected from extracts by MALDI MS.[72] It has been shown that the rhamnolipid profile can vary greatly with bacterial strain and growth conditions,[75] thus it is reasonable to assert that the particular *P. aeruginosa* strain and

conditions studied here did not produce the other rhamnolipid species in significant (detectable) abundance. Furthermore, the MS data confirm and extend the conclusions drawn from the differences in Raman scattering highlighted between Figs. 1 and 2. The assignment of Raman bands at 1030 cm^{-1}, 1068 cm^{-1} and 1155 cm^{-1} to rhamnolipids is confirmed by MS identification of a series of specific congeners from the rhamnolipid family.

MALDI MS imaging of the wild-type *P. aeruginosa* biofilm allowed visualization of specific rhamnolipids, which generally exhibited a heterogeneous distribution over the sample surface. Furthermore, while the individual rhamnolipid distributions share some resemblance, they are not identical; for example, monorhamnolipid Rha-C8-C10 (m/z 499.4) and dirhamnolipid Rha-Rha-C10-C12 (m/z 701.6) ion images shown in Fig. 5 show overlapping but distinct distributions, with exclusive regions of localization in the opposite corners of the substrate. Dirhamnolipids have been shown to act as chemoattractants in swarming motility of *P. aeruginosa*, while monorhamnolipids do not,[76] so the differential distributions observed here may relate to these unique roles in biofilm development. Furthermore, the genes responsible for mono- and dirhamnolipid synthesis (*rhlB* and *rhlC*, respectively) are located in different operons and synthesis of dirhamnolipids occurs by addition of a second rhamnose to existing monorhamnolipids. Thus, the observed difference in spatial distributions could arise from temporal differences in expression during biofilm growth and maturation.[73] Another interesting feature of the wild-type biofilm is the association of small light-colored regions with localization of dirhamnolipid Rha-Rha-C10-C12, but not monorhamnolipid Rha-C8-C10; the nature of these features is not understood and is currently under investigation.

Conclusions

CRM and MSI have been combined to characterize chemical composition and structure in samples of *P. aeruginosa* – both planktonic cells and biofilms, as well as the changes that accompany biofilm formation when comparing a wild type to a QS (Δ*las*Δ*rhlI*) mutant strain incapable of producing either rhamnolipids or the homo-serine lactones used in quorum sensing. Raman analysis of wild type planktonic cells reveal spectra that are dominated by DNA/RNA-related spectral features – bands that are almost completely absent in the biofilm. Instead biofilms produce spectra that are dominated by rhamnolipids, secreted as part of the biofilm formation process, and by a co-secreted protein/peptide component. In contrast, the QS mutant exhibits very similar spectra to the planktonic cells after 72 h under the same conditions used to obtain the wild-type biofilms. The straightforward interpretation of these observations posits the formation of a thick (relative to the sampling depth of the CRM) biofilm after 72 h in the wild type cells, but not in the QS mutant. MALDI MS profiling was applied to obtain more chemically specific information on the variety of rhamnolipids present; nine putative rhamnolipid species were detected in the wild-type biofilm, six of which could be confirmed by tandem MS. Furthermore, MS imaging revealed that rhamnolipid distributions were heterogeneous across the wild-type biofilm, consistent with the variegation observed at higher spatial resolution in the biofilm Raman image, Fig. 3(b), and also showed differences which may relate to differential expression and/or function of specific congeners and homologs within the rhamnolipid class; future work will further elucidate this observation and characterize temporal changes during biofilm development.

Acknowledgement

This work was supported by the Department of Energy Office of Biological and Environmental

Research through grant DE SC0006642.

References

1. H. F. Jenkinson and H. M. Lappin-Scott, *Trends Microbiol.*, 2001, **9**, 9-10.

2. H. C. Flemming, *Appl. Microbiol. Biotechnol.*, 2002, **59**, 629-640.

3. S. S. Branda, A. Vik, L. Friedman and R. Kolter, *Trends Microbiol.*, 2005, **13**, 20-26.

4. D. Lopez, H. Vlamakis and R. Kolter, *Cold Spring Harbor Perspectives in Biology*, 2010, **2**, a000398.

5. M. Rodgers, G. X. Wu and X. M. Zhan, *J. Environm. Qual.*, 2008, **37**, 977-982.

6. N. Qureshi, B. A. Annous, T. C. Ezeji, P. Karcher and I. S. Maddox, *Microbial Cell Factories*, 2005, **4**:24.

7. J. C. Nickel, I. Ruseska, J. B. Wright and J. W. Costerton, *Antimicrob. Agents Chemother.*, 1985, **27**, 619-624.

8. E. Drenkard, *Microb. Infect.*, 2003, **5**, 1213-1219.

9. M. Schuster, C. P. Lostroh, T. Ogi and E. P. Greenberg, *J. Bacteriol.*, 2003, **185**, 2066-2079.

10. V. E. Wagner, D. Bushnell, L. Passador, A. I. Brooks and B. H. Iglewski, *J. Bacteriol.*, 2003, **185**, 2080-2095.

11. J. W. Costerton, Z. Lewandowski, D. E. Caldwell, D. R. Korber and H. M. Lappinscott,

Ann. Rev. Microbiol., 1995, **49**, 711-745.

12. F. F. Dias and J. V. Bhat, *Appl. Microbiol.*, 1964, **12**, 412-417.

13. K. S. Jorgensen and A. S. L. Pauli, *Anaerobe*, 1995, **1**, 161-168.

14. U. Szewzyk, R. Szewzyk, W. Manz and K. H. Schleifer, *Ann. Rev. Microbiol.*, 2000, **54**, 81-127.

15. D. G. Davies, M. R. Parsek, J. P. Pearson, B. H. Iglewski, J. W. Costerton and E. P. Greenberg, *Science*, 1998, **280**, 295-298.

16. M. R. Parsek and E. P. Greenberg, *Biofilms*, 1999, **310**, 43-55.

17. J. M. Brint and D. E. Ohman, *J. Bacteriol.*, 1995, **177**, 7155-7163.

18. P. R. Hsueh, L. J. Teng, P. C. Yang, Y. C. Chen, S. W. Ho and K. T. Luh, *J. Clin. Microbiol.*, 1998, **36**, 1347-1351.

19. R. Y. Hachem, R. F. Chemaly, C. A. Ahmar, Y. Jiang, M. R. Boktour, G. Abou Rjaili, G. P. Bodey and I. I. Raad, *Antimicrob. Agents Chemother.*, 2007, **51**, 1905-1911.

20. P. Ashorn, B. Moss, J. N. Weinstein, V. K. Chaudhary, D. J. Fitzgerald, I. Pastan and E. A. Berger, *Proc. Natl. Acad. Sci. USA*, 1990, **87**, 8889-8893.

21. U. Romling, B. Fiedler, J. Bosshammer, D. Grothues, J. Greipel, H. Vonderhardt and B. Tummler, *J. Infect. Dis.*, 1994, **170**, 1616-1621.

22. L. Passador, J. M. Cook, M. J. Gambello, L. Rust and B. H. Iglewski, *Science*, 1993, **260**, 1127-1130.

23. J. W. Costerton, P. S. Stewart and E. P. Greenberg, *Science*, 1999, **284**, 1318-1322.

24. J. D. Morris, J. L. Hewitt, L. G. Wolfe, N. G. Kamatkar, S. M. Chapman, J. M. Diener, A. J. Courtney, W. M. Leevy and J. D. Shrout, *Appl. Environ. Microbiol.*, 2011, **77**, 8310-8317.

25. N. Kamatkar and J. Shrout, *PLoS One*, 2011, **6**, e20888.

26. S. Chugani, B. Kim, S. Phattarasukol, M. Brittnacher, S. Choi, C. Harwood and E. Greenberg, *Proc. Natl. Acad. Sci. U S A.*, 2012, **109**, E2823-E2831.

27. S. Pamp and T. Tolker-Nielsen, *J. Bacteriol.*, 2007, **189**, 2531-2539.

28. X. Latour, T. S. Corberand, G. Laguerre, F. Allard and P. Lemanceau, *Appl. Environ. Microbiol.*, 1996, **62**, 2449-2456.

29. A. Camilli and B. L. Bassler, *Science*, 2006, **311**, 1113-1116.

30. M. E. Davey and G. A. O'toole, *Microbiol. Mol. Biol. Rev.*, 2000, **64**, 847-867.

31. G. A. O'Toole and R. Kolter, *Mol. Microbiol.*, 1998, **28**, 449-461.

32. X. Zhang, M. B. J. Roeffaers, S. Basu, J. R. Daniele, D. Fu, C. W. Freudiger, G. R. Holtom and X. S. Xie, *Chemphyschem*, 2012, **13**, 1054-1059.

33. S. H. Yue, J. M. Cardenas-Mora, L. S. Chaboub, S. A. Lelievre and J. X. Cheng, *Biophys. J.*, 2012, **102**, 1215-1223.

34. A. Barhoumi and N. J. Halas, *J. Am. Chem. Soc.*, 2010, **132**, 12792-12793.

35. R. M. Jarvis and R. Goodacre, *Chem. Soc. Rev.*, 2008, **37**, 931-936.

36. A. Harz, P. Rosch and J. Popp, *Cytom. A*, 2009, **75A**, 104-113.

37. W. E. Huang, R. I. Griffiths, I. P. Thompson, M. J. Bailey and A. S. Whiteley, *Analyt. Chem.*, 2004, **76**, 4452-4458.

38. N. P. Ivleva, M. Wagner, H. Horn, R. Niessner and C. Haisch, *J. Biophoton.*, 2010, **3**, 548-556.

39. C. Sandt, T. Smith-Palmer, J. Pink, L. Brennan and D. Pink, *J. Appl. Microbiol.*, 2007, **103**, 1808-1820.

40. K. Maquelin, C. Kirschner, L. P. Choo-Smith, N. van den Braak, H. P. Endtz, D. Naumann and G. J. Puppels, *J. Microbiol. Methods*, 2002, **51**, 255-271.

41. S. A. Overman, K. L. Aubrey, K. E. Reilly, O. Osman, S. J. Hayes, P. Serwer and G. J. Thomas, *Biospectroscopy*, 1998, **4**, S47-S56.

42. C. Krafft, T. Knetschke, A. Siegner, R. H. W. Funk and R. Salzer, *Vib. Spectrosc.*, 2003, **32**, 75-83.

43. S. Rubakhin and J. Sweedler, in *Mass Spectrometry Imaging*, eds. S. S. Rubakhin and J. V. Sweedler, Humana Press, 2010, vol. 656, ch. 2, pp. 21-49.

44. K. Chughtai and R. M. A. Heeren, *Chem. Rev.*, 2010, **110**, 3237-3277.

45. E. J. Lanni, S. S. Rubakhin and J. V. Sweedler, *J. Proteom.*, 2012, **75**, 5036-5051.

46. V. V. Phelan, W.-T. Liu, K. Pogliano and P. C. Dorrestein, *Nat. Chem. Biol.*, 2012, **8**, 26-35.

47. M. Blaze M. T, B. Aydin, R. P. Carlson and L. Hanley, *Analyst*, 2012, **137**, 5018-5025.

48. S. Vaidyanathan, J. S. Fletcher, R. Goodacre, N. P. Lockyer, J. Micklefield and J. C. Vickerman, *Anal. Chem.*, 2008, **80**, 1942-1951.

49. J. D. Watrous and P. C. Dorrestein, *Nat. Rev. Micro.*, 2011, **9**, 683-694.

50. R. Masyuko, E. Lanni, J. Sweedler and P. Bohn, *Analyst*, 2013, **138**, 1924-1939.

51. Z. Li, L. Chu, J. Sweedler and P. Bohn, *Anal. Chem.*, 2010, **82**, 2608-2611.

52. L. Zhang, T. A. Veres-Schalnat, A. Somogyi, J. E. Pemberton and R. M. Maier, *Appl. Environ. Microbiol.*, 2012, **78**, 8611-8622.

53. A. Lebron-Paler, J. E. Pemberton, B. A. Becker, W. H. Otto, C. K. Larive and R. M. Maier, *Analyt. Chem.*, 2006, **78**, 7649-7658.

54. J. D. Shrout, D. L. Chopp, C. L. Just, M. Hentzer, M. Givskov and M. R. Parsek, *Mol. Microbiol.*, 2006, **62**, 1264-1277.

55. A. Heydorn, A. T. Nielsen, M. Hentzer, C. Sternberg, M. Givskov, B. K. Ersboll and S. Molin, *Microbiology (UK),* 2000, **146**, 2395-2407.

56. A. Haase, H. F. Arlinghaus, J. Tentschert, H. Jungnickel, P. Graf, A. Mantion, F. Draude, S. Galla, J. Plendl, M. E. Goetz, A. Masic, W. Meier, A. F. Thunemann, A. Taubert and A. Luch, *ACS Nano*, 2011, **5**, 3059-3068.

57. B. Pei and J. W. Chen, *J. Biochem.*, 2003, **134**, 575-581.

58. I. Notingher, S. Verrier, H. Romanska, A. E. Bishop, J. M. Polak and L. L. Hench, *Spectroscopy*, 2002, **16**, 43-51.

59. M. Harz, P. Rosch, K. D. Peschke, O. Ronneberger, H. Burkhardt and J. Popp, *Analyst*,

2005, **130**, 1543-1550.

60. U. Neugebauer, U. Schmid, K. Baumann, W. Ziebuhr, S. Kozitskaya, V. Deckert, M. Schmitt and J. Popp, *Chemphyschem*, 2007, **8**, 124-137.

61. N. Uzunbajakava, A. Lenferink, Y. Kraan, B. Willekens, G. Vrensen, J. Greve and C. Otto, *Biopolymers*, 2003, **72**, 1-9.

62. G. J. Puppels, H. S. P. Garritsen, G. M. J. Segersnolten, F. F. M. Demul and J. Greve, *Biophys. J.*, 1991, **60**, 1046-1056.

63. R. Manoharan, E. Ghiamati, S. Chadha, W. H. Nelson and J. F. Sperry, *Appl. Spectrosc.*, 1993, **47**, 2145-2150.

64. K. Maquelin, L. P. Choo-Smith, T. van Vreeswijk, H. P. Endtz, B. Smith, R. Bennett, H. A. Bruining and G. J. Puppels, *Analyt. Chem.*, 2000, **72**, 12-19.

65. D. Herbert, *Symp. Soc. Gen. Microbiol.*, 1961, **11**, 391-416.

66. M. Jadhav, S. Kalme, D. Tamboli and S. Govindwar, *J. Basic Microbiol.* , 2011, **51**, 385-396.

67. B. R. Boles, M. Thoendel and P. K. Singh, *Mol. Microbiol.*, 2005, **57**, 1210-1223.

68. M. E. Davey, N. C. Caiazza and G. A. O'Toole, *J. Bacteriol.*, 2003, **185**, 1027-1036.

69. J. P. Pearson, E. C. Pesci and B. H. Iglewski, *J. Bacteriol.*, 1997, **179**, 5756-5767.

70. A. F. M. Altelaar, I. Klinkert, K. Jalink, R. P. J. de Lange, R. A. H. Adan, R. M. A. Heeren and S. R. Piersma, *Analyt. Chem.*, 2005, **78**, 734-742.

71. Z. Li, P. W. Bohn and J. V. Sweedler, *Bioresour. Technol.*, 2010, **101**, 5578-5585.

72. N. P. J. Price, K. J. Ray, K. Vermillion and T.-M. Kuo, *Carbohydr. Res.*, 2009, **344**, 204-209.

73. A. Abdel-Mawgoud, F. Lépine and E. Déziel, *Appl. Microbiol. Biotechnol.*, 2010, **86**, 1323-1336.

74. C. G. de Koster, B. Vos, C. Versluis, W. Heerma and J. Haverkamp, *Bio. Mass Spectrom.*, 1994, **23**, 179-185.

75. M. Rikalovic, A. Abdel-Mawgoud, E. Déziel, G. Gojgic-Cvijovic, Z. Nestorovic, M. Vrvic and I. Karadzic, *J. Surfact. Deterg.*, 2013, **16**, 673-682.

76. J. Tremblay, A.-P. Richardson, F. Lépine and E. Déziel, *Environ. Microbiol.*, 2007, **9**, 2622-2630.

Figures

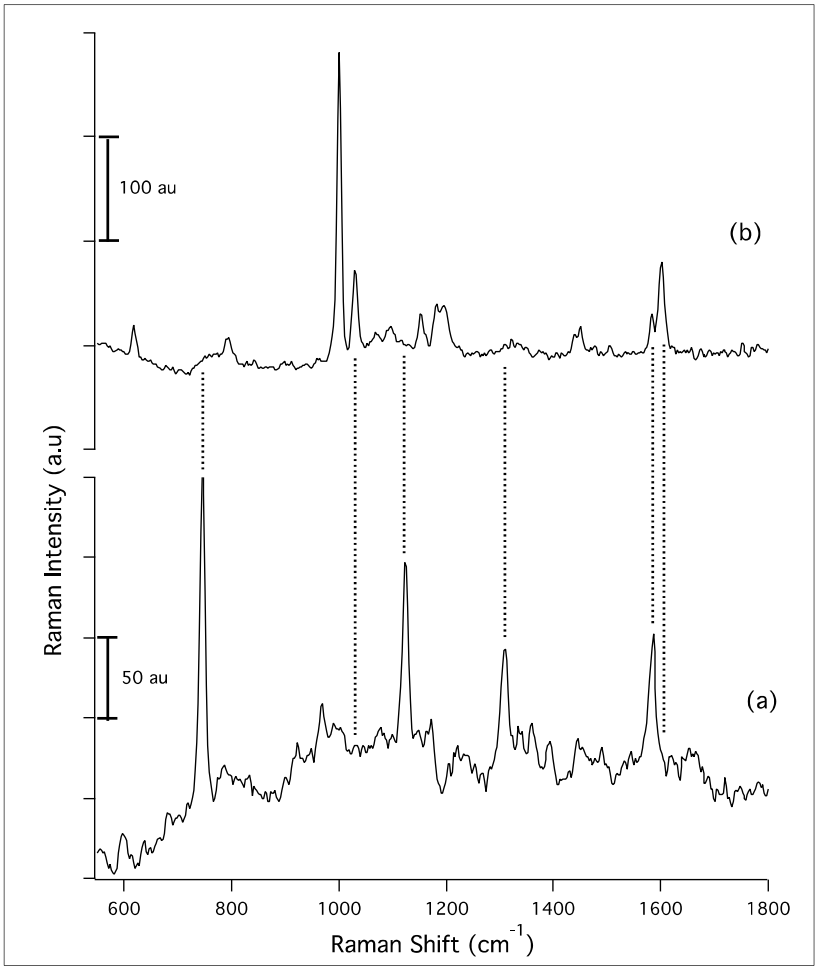

Figure 1. Raman microspectra of wild type *Pseudomonas aeruginosa*. (a) Planktonic cells, as deposited on Au-coated Si substrate. (b) Biofilm after 72 h formation on uncoated Si. Raman spectra are baseline corrected using a fourth order polynomial function. Vertical dashed lines added to aid comparison between spectra.

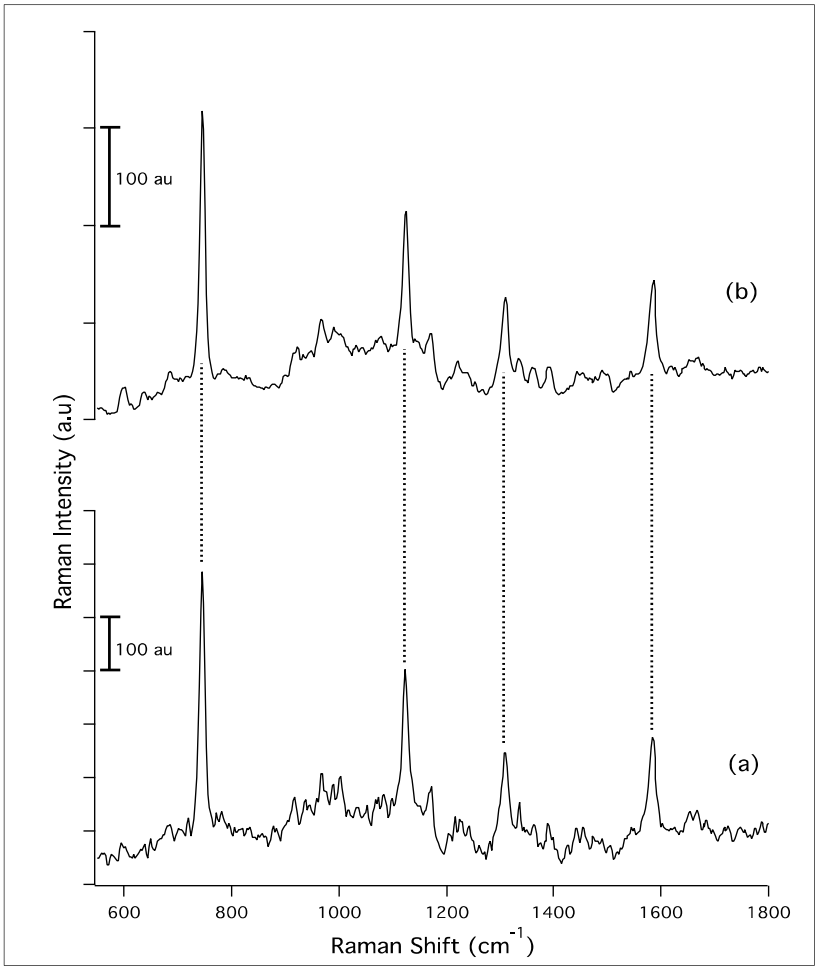

Figure 2. Raman microspectra of Δ*las*Δ*rhlI* mutant (MH710) *Pseudomonas aeruginosa*. (a) Planktonic cells as deposited on Au-coated Si substrate. (b) Same cells after 72 h in conditions supporting biofilm formation in the wild type. Raman spectra are baseline corrected using a fourth order polynomial function. Vertical dashed lines added to aid comparison between spectra.

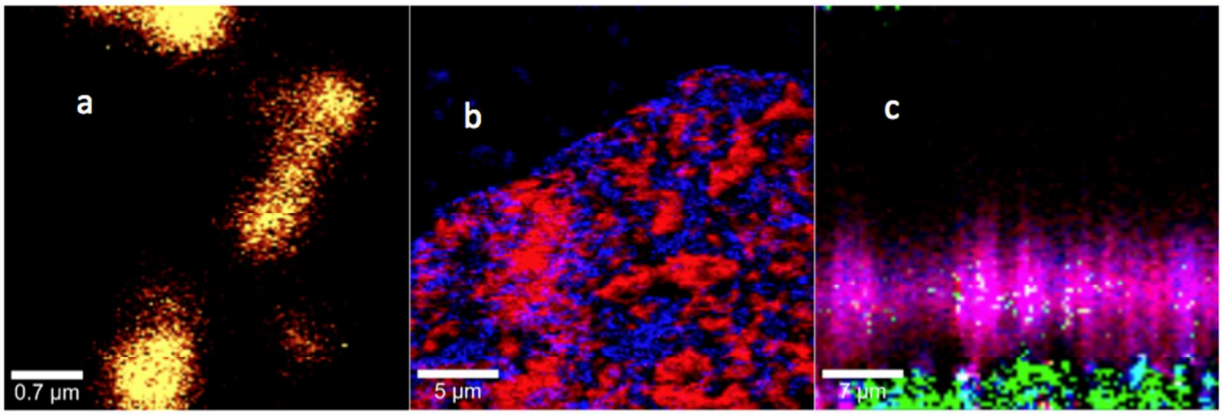

Figure 3. Composite Raman images of different *Pseudomonas aeruginosa* samples. (a) Plan view image of planktonic cells constructed from scattering in the region 2800-3050 cm^{-1}. Scale bar 0.7 µm. (b) Plan view image of a biofilm constructed from a combination of bands in the regions 1560-1620 cm^{-1} (red) and 1010-1165 cm^{-1} (blue), characteristic of protein and carbohydrate scattering, respectively. Scale bar 5 µm. (c) Depth profile of the biofilm in the *x-z* plane constructed from 2800-3050 cm^{-1} (red), 1560-1620 cm^{-1} (blue) and 725-775 cm^{-1} (green). Scale bar 7 µm.

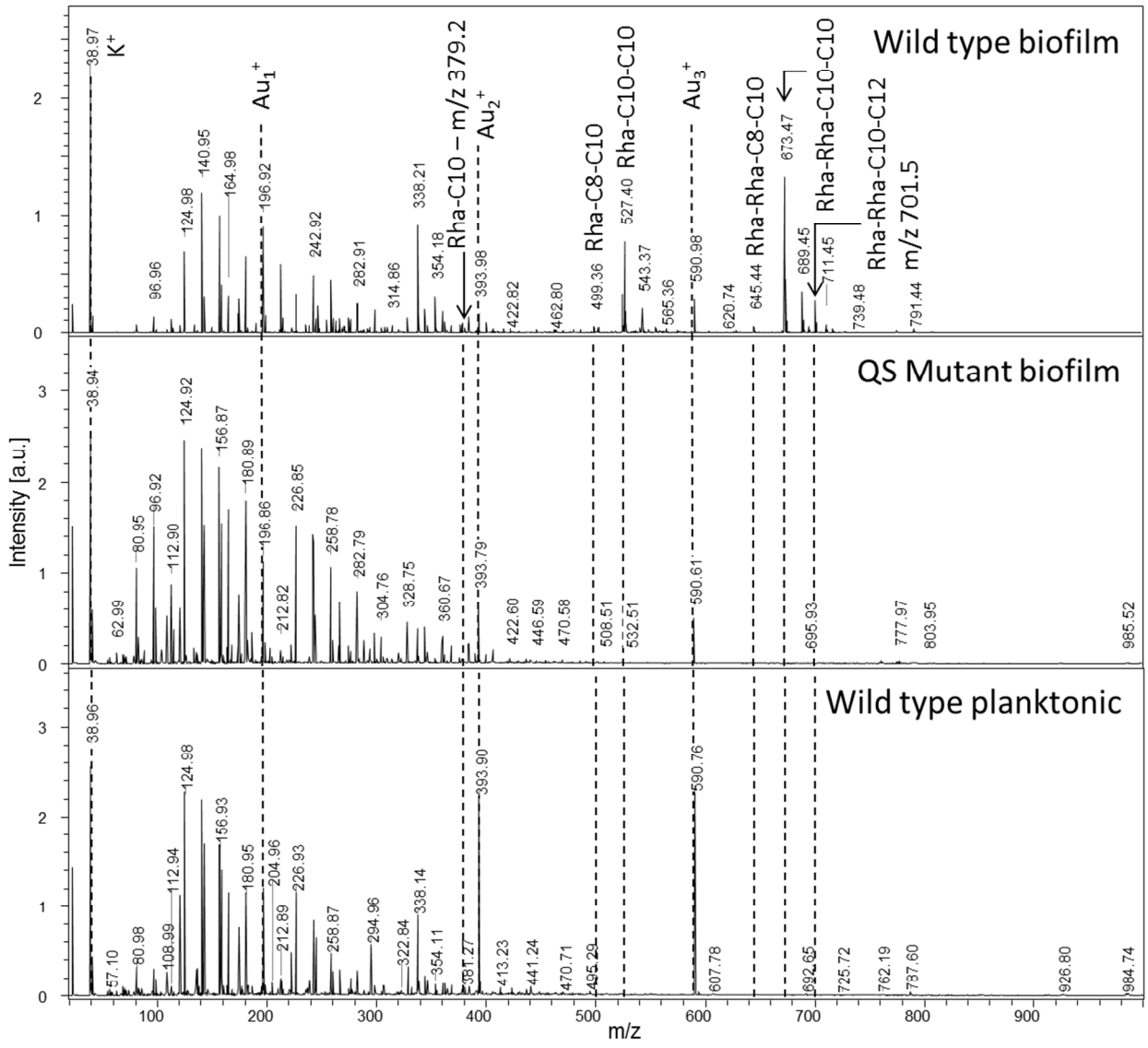

Figure 4. Representative MALDI MS single-pixel spectra of *P. aeruginosa* wild-type biofilm (*top*), QS mutant biofilm (*center*), and wild-type planktonic cells (*bottom*). Rhamnolipid-derived ions are detected exclusively in the wild-type biofilm.

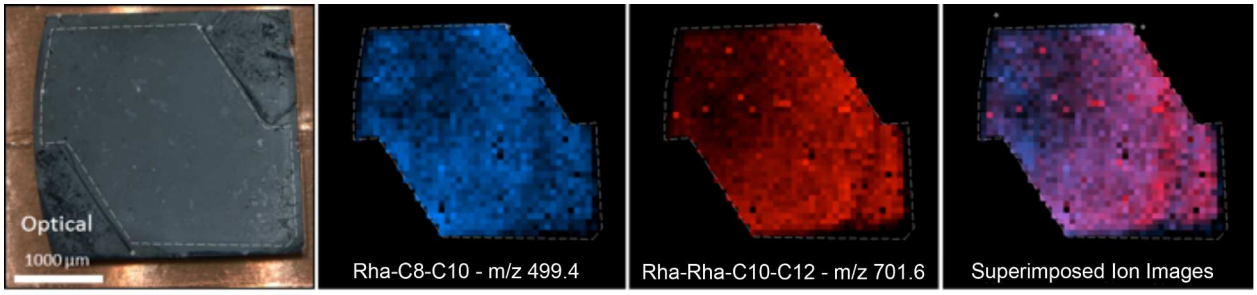

Figure 5. *P. aeruginosa* wild type biofilm optical (*left*) and rhamnolipid ion (*center and right*) images with Rha-C8-C10 (blue) and Rha-Rha-C10-C12 (red) color coded, scale bar 1 mm. Superposition of the mono- and dirhamnolipid reveals non-uniform distribution patterns, and dirhamnolipid Rha-Rha-C10-C12 also appear highly localized to small biofilm features.

Compound	Molecular Formula	$[M+Na]^+$ theor.	$[M+Na]^+$ obs.	MS/MS confirmation
Rha-C10	$C_{16}H_{30}O_7$	379.2*	379.2*	Y
Rha-C8-C10	$C_{24}H_{44}O_9$	499.3	499.4	Y
Rha-Rha-C10	$C_{22}H_{40}O_{11}$	503.3	503.4	
Rha-C10-C10	$C_{26}H_{48}O_9$	527.3	527.4	Y
Rha-C10-C12:1	$C_{28}H_{50}O_9$	553.3	553.4	
Rha-C10-C12	$C_{28}H_{52}O_9$	555.4	555.5	
Rha-Rha-C8-C10	$C_{30}H_{54}O_{13}$	645.3	645.4	Y
Rha-Rha-C10-C10	$C_{32}H_{58}O_{13}$	673.4	673.5	Y
Rha-Rha-C10-C12	$C_{34}H_{62}O_{13}$	701.4	701.5	Y

Table 1 – Rhamnolipid species detected on *P. aeruginosa* wild type biofilm and successfully identified by *in situ* tandem MS. *Rha-C10 detected as $[M-H+2Na]^+$

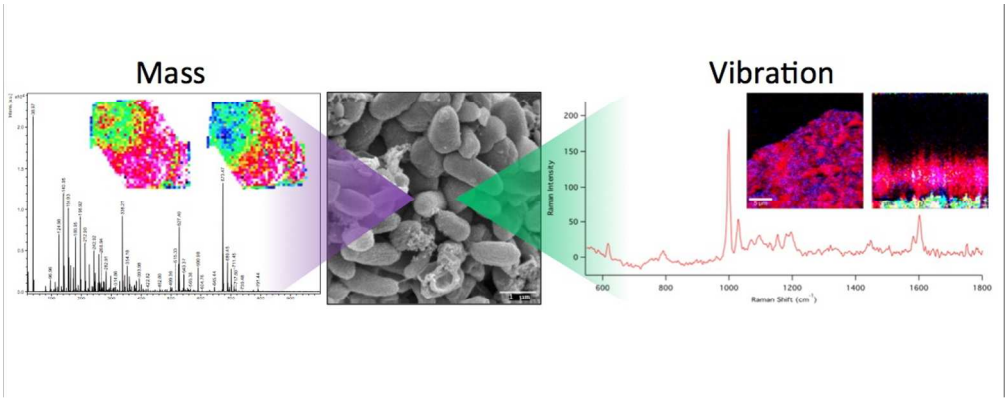

424x166mm (72 x 72 DPI)